Chapter 1.12. $W_{1-x}Mo_xO_3*0.33H_2O$ Compounds Synthetized by Hydrothermal and Microwave-radiation for H_2 Production

A. Arzola-Rubio; J. Camarillo-Cisneros; V. Collins-Martínez*

Centro de Investigación en Materiales Avanzados S. C., Miguel de Cervantes 120, C. P. 31136, Chihuahua, Chih. México

ABSTRACT

WO_3 has been thoroughly investigated and optimized to deliver high single wavelength quantum efficiencies. Unfortunately the stability of this oxide in aqueous environments, aided by an energetically low valence band which is defined largely by O 2p energy levels, also brings a large band gap which renders these materials transparent to most of the incident solar illumination. A series of hydrated Tungsten-Molybdenum oxides have been synthesized by hydrothermal and microwave radiation techniques. In both cases the $WO_3 \cdot 0.33H_2O$ crystal lattice can be substituted with up to 75% Mo without structural alterations of the orthorhombic host structure. These products have a band gap suited at the visible range (~2.00 eV). Experimental data were explained by means of first-principle calculations in the framework of DFT and DFT+U; indirect semiconductors were obtained. Both compounds were evaluated for H_2 production.

Keywords: H_2 generation; water splitting; photocatalysis; tungstates

1. Introduction

Hydrogen is considered as an ideal energetic vector for the future. Hydrogen fuel can be produced from clean and renewable energy sources and, thus, its life cycle is clean and renewable. Solar and wind are the two major sources of renewable energy and they are also the promising sources for renewable hydrogen production. However, presently, renewable energy contributes only about 5% of the commercial hydrogen production primarily via water electrolysis, while other 95% hydrogen is mainly derived from fossil fuels [1]. Renewable hydrogen production is not popular yet because the cost is still high.

Photovoltaic water electrolysis may become more competitive as the cost continues to decrease with the technology advancement; however, the considerable use of small band gap semiconducting materials may cause serious life cycle environmental impacts.

---

* Author for correspondence: V. Collins Martinez, T: +526144391129; E: virginia.collins@cimav.edu.mx

Alternatively, photocatalytic water-splitting using unary and binary WO_3 compounds for hydrogen production offers a promising way for clean, low-cost and environmentally friendly production of hydrogen by solar energy. WO_3 compounds can be used for photocatalytic water splitting to produce hydrogen gas using visible solar light, because of its narrow bandgap. Earlier studies of the photo electrochemical behavior of both polycrystalline and monocrystalline WO_3 provided instructive knowledge for the development of photocatalytic water-splitting systems [2, 3]. The difficulty in the overall water splitting (both reduction and oxidation of H_20 molecules are to be achieved) by WO_3 is that the lower edge of the CB lies below the redox potential of H_20/H_2. This means that the reduction of water molecules to generate hydrogen gas is thermodynamically unfavorable [4]. Applying a bias potential to the system can overcome the energy barrier for the photogenerated electrons to be ejected into the adsorbed water molecules [5]. Coupling with other semiconductor materials [6] and doping by metal ions [7] are other alternatives to make use of the oxidation power of WO_3 for water splitting. WO_3 also found interesting applications in electrochromic [8] and photochromic [9] devices such as large area displays and "smart windows" because WO_3 films can be switched between different optical states under different electro-chemical or optical conditions. The electrochromic effect is caused by the electrochemical reaction between the WO_3 electrode and protons in the electrolyte solution, under the influence of a bias potential to provide charge carriers (electrons in this case). The electrons can then create color centers by reducing the W^{6+} species to W^{5+} species. The photochromism effect of WO_3 is due to the formation of an identical absorption band upon light irradiation. This process is completely reversible by exposing the reduced sample to oxygen gas. DFT has been a handy tool to corroborate gap experimental data and also as a method itself to use in simulate tendencies. Recently, Zhou et al., [10] was capable of modulate the band gaps of the $W_{1-x}Mo_xO_3$ materials by changing the Mo/W ratio. They successfully prepared a series of $W_{1-x}Mo_xO_3*0.33H_2O$ micro/nanostructures with controlled stoichiometry (x = 0, 0.25, 0.50, 0.75). They stated that the increase of the Mo content, the band gap of $W_{1-x}Mo_xO_3*0.33H_2O$ narrowed from 3.25 to 2.77 eV.

In this work we synthetized a series of $W_{1-x}Mo_xO_3*0.33H_2O$ nano/microstructures similar to Zhou et al. [10] from other precursors such as ammonium heptamolybdate and ammonium metatungstate instead of metal powders. We used 2.2M HNO_3 to acidify the solutions instead of forming the peroxopolytungstic and molybdic acid solutions. Our primary objective was to study their enhanced band gaps as a function of the Mo content and its capability of photocatalytically hydrogen production.

2. Experimental

For a usual synthesis, y mmol (y = 0, 2.5, 5.0, 7.5, and 10.0) of Ammonium heptamolybdate tetrahydrate and (10 - y) mmol of Ammonium metatungstate hydrate were dissolved in a mixture of 21 mL of H_2O, 9 mL of 30 wt.% H_2O_2 , and 3 mL of 2.2M HNO_3. The solution was then transferred into a Teflon vial then placed in a stainless-steel autoclave and, sealed, and hydrothermally treated at 180°C for 24 h. The solid solutions were collected by centrifugation, washed with deionized water 3 times, and dried at room

temperature. For the microwave synthesis, the reactants are the same just the quantities vary. There were dissolved in a mixture of 9 mL of tridistilled H_2O, 4 mL of 30 wt. % H_2O_2, and 1.5 mL of 2.2 M HNO_3. Each solution was then transferred into a Teflon vial and placed in an EasyPrep vessel inside a CEM MARS 6 microwave, sealed and hydrothermally treated at 200 °C with a heat ramp of 15 min (13°C/min) and 5 min plateau with a 20 min total time heating. The resultant products with y = 0, 2.5, 5.0, 7.5, and 10.0 were designated as WH1 (WO_3*0.33H_2O) for hydrothermal and WH1m for MW synthesis; WM25 ($W_{0.75}Mo_{0.25}O_3$*0.33H_2O) for hydrothermal and WM25m for MW; WM50 ($W_{0.50}Mo_{0.50}O_3$*0.33H_2O) for hydrothermal and WM25m for MW; WM75 ($W_{0.25}Mo_{0.75}O_3$*0.33H_2O) for hydrothermal and WM75m for MW and MH1 (MoO_3*0.55H_2O) for hydrothermal and MH1m for MW, respectively.

X-ray diffraction (XRD) patterns were recorded on a Philips X'Pert MPD X-ray Diffractometer with Cu KR radiation (ƛ=1.54056 Å) at 40 kV and a current of 30 mA. Scanning electron microscopy (SEM) images were obtained on a cold field emission JEOL JSM-7401F microscope operated at 5 and 17 kV. An energy-dispersive X-ray spectroscopy (EDS) facility (Oxford INCA X-Sight) attached to the SEM was employed to analyze the chemical composition. UV-vis diffusive reflectance spectra (DRS) were obtained on a Lambda 9 UV-vis spectrometer. The Brunauer-Emmett-Teller (BET) surface areas were measured on a nitrogen adsorption apparatus (Quadrasorb SI, Quantachrome). The samples were degassed at 150-250°C for 12 h before the measurement. All ab-initio calculations were performed using the Quantum Espresso code in the framework of density functional theory (DFT). Due to the known band gap sub-estimation in DFT treatments (by the presence of "d" orbitals in W and Mo) DFT+U method was employed. The models for calculating WH1 and MH1 oxides were to reduce the unit cells from conventional to primitive, while the bimetallic solutions (WM25, WM50 and WM75) were calculated by means of 2x2x1 supercells. In all systems, the hydrated unit cell were employed (to XRD pattern fitting and to DFT calculations), however in both theoretical approach the H atoms are excluded. Hydrogen production was monitored using a gas chromatography Perkin Elmer, Clarus 500, a batch quartz photoreactor and a 250 W mercury lamp (Figure 1).

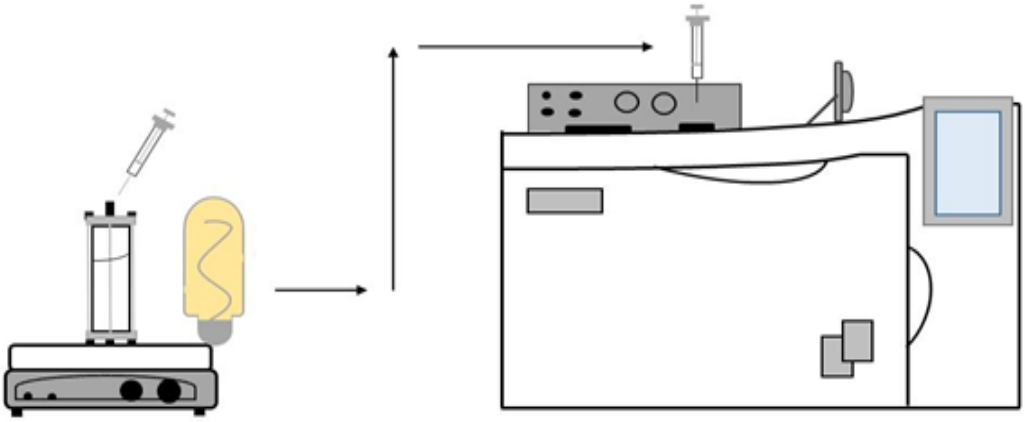

Fig. 1. Scheme of the photocatalytic evaluation system.

3. Results and discussion

All XRD patterns are included in Figure 2. For WH1 the indexing corresponds to orthorhombic crystal, space group Aba2 and lattice parameters a = 7.323Å, b=7.690Å, c=12.772Å (calculated from ICSD using POWD- 12++ 228, 695 (1997)). For Mo fraction x = 0:25; 0:50, and 0:75 the space group was maintained, indicating that W in WO_3*0.33H_2O can be substituted up to 75% by Mo. According to the references [11,12] the appearance of new diffraction peaks in this case is due to the reduced symmetry from an F-centered orthorhombic cell for WO_3*0.33H_2O to a C-centered orthorhombic cell for $W_{0.25}Mo_{0.75}O_3$*0.33H_2O caused by increased distortions induced by Mo substitution. For MH1 (x = 1.00), the XRD pattern can be assigned to hexagonal MoO_3*0.55H_2O (calculated from ICSD using POWD- 12++ 228, 695 (1997), space group P63/m, lattice parameters a= 1.0584 nm, b = 1.0584 nm, c = 0.3727 nm).

Figure 3 (I) represents the SEM images of the solid solutions of the hydrothermal synthesis. For WH1 (a), WM25 (b), WM50 (c) and WM75 (d), the products are mainly composed of nanometer sized flakes (200 nm in size). We can observe micro irregular particles for MH1 (e) with widths and lengths of approximately 29000±15000 nm. Measurements values can be found in Table 1. SEM micrographs in Figure (II) shows synthetized solid solutions by microwave radiation of WH1m (a) that has a particle size of 104 nm and regular and elongated hexagonal-like morphology, WM25m (b) and WM50m (c) have an average particle size of 195 nm with regular hexagonal-like morphology, WM75m (d) has irregular morphology and particle size of 1500 nm, and MH1m (e), the products are mainly composed of micro meter particles of 6600 ± 5100 nm.

It can be observed, between more Mo atoms enters to the crystalline lattice, the particle is bigger. Figure 3(III) shows bright field transmission electron micrographs for materiales synthetized hydrothermally. The first four images show ”hexagonal” flake-like morphologies with a length and width of around 600 nm and 150 nm, respectively. For sample MH1, we observe micrometric size particles with an irregular hexagonal rod shape. Micrographs obtained at low magnification correspond to TEM micrographs at Figure 3 (IV) for all chemical compositions (WH1m-WM75m) obtained with microwave radiation. Micrographs from Figure 3-IV(a,c,e,g) show hexagonal flakes morphology with average lengths of ~100nm and widths of ~150nm.

From the absorption spectra of the samples (hydrothermal and microwave), it is under study that substitution shifts the absorption edge of $W_{1-x}Mo_xO_3$*0.33H_2O from the UV to visible region (Figure 4 a-b). Now, we can determine the effective reduction in the band gap (BG) of these solid solutions due to the incorporation of Mo. The line drawn on the linear part of $[F(R)h\gamma]^{1/2}$ vs. hν curve at $[F(R)h\gamma]^{1/2} = 0$ gives the band gap.

In pure WO_3, the electronic transition occurs directly from VB to CB. For the W/Mo samples, the results are rather similar to that of WO_3 0.33H_2O except that they show more absorption in the visible range (~440 nm). With the introduction of 25% of Mo, a significant shift can be observed (compared against WO_3*0.33H_2O), indicating a narrowing of the band gap. With even more Mo fraction, shifts can be observed.

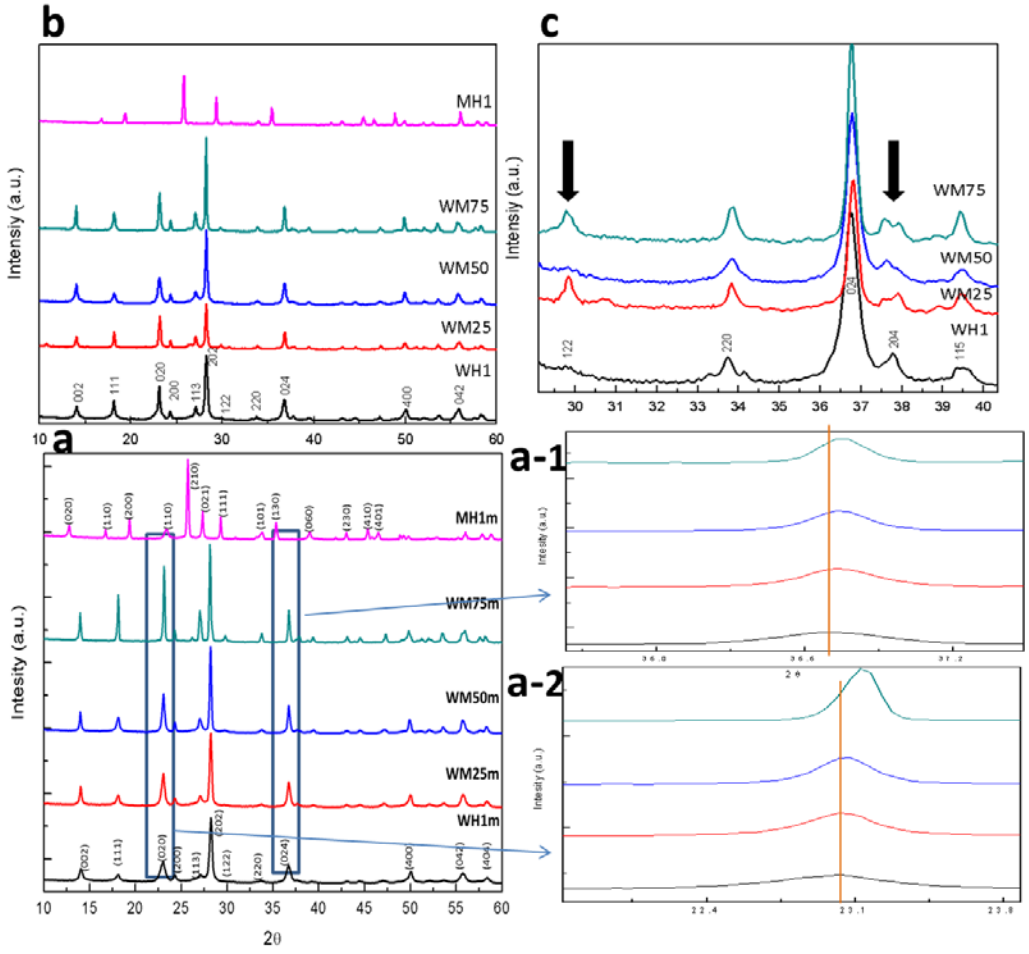

Fig. 2. (a) XRD patterns of compounds synthetized by microwave radiation; (a-1 and a-2) Zoom of peaks at 2θ = 23 and 2θ = 36. F; (b) XRD patterns of compounds synthetized by hydrothermal synthesis; (c) Appearing and splitting of peaks at 2θ = 30 and 2θ = 38

Table1. Theoretical and experimental Mo content, BET surface area and band gap.

		EDS MW	**EDS hydro**	**BG hydro**	**BG MW**	**BG hydro**	**SP MW**
Sample	$X_{theorical}$ [1]	X_{EDS} [2]	X_{EDS} [2]	Eg (eV) [5]	Eg (eV) [5]	Particle size (nm)	Particle size (nm)
WH1m	0	0	0	2.4	2.55	104±51	73±35
WM25m	25	6.3	21	1.95	2.37	192±52	337±223
WM50m	50	9.3	37	1.93	2.35	202±99	103±65
WM75m	75	57.0	55	1.90	2.15	1500±470	163±57
MH1m	100	100	100	2.3	2.25	6600±5100	4500±15000

[1]Theoretical Mo content, [2]Mo content of hydrothermal and microwave synthesis determined from EDS, [4]Band gap of compounds synthetized by microwave radiation, [5]Band Gap of compounds synthetized by hydrothermal synthesis.

For x = 0.25, 0.50, and 0.75, the band gaps of the solid solutions are 2.37, 2.35, and 2.15 eV for hydrothermal and for microwave radiation the values are 1.95, 1.93 and 1.90 eV. The band gap of MH1 and MH1m, which is 2.25 and 2.30 eV respectively, does not follow the trend of the $W_{1-x}Mo_xO_3$*0.33H_2O solid solutions due to its structural difference. We believe that the narrowing of the BG is because of the additional fraction of Mo as Zhou et al. [10] stated: "The increased M^{5+} fraction and thus enhanced intervalency-transition are responsible for the narrowing of the band gap".

DFT calculations resulted in decrease of the electronic gap in function of Mo addition, going from 0.491, 0.435, 0.433 and 0.418 eV to WH1, WM25, WM50 and WM75 respectively. However metallic character was obtained in MH1 compound; in disagree to experimental measured value. The gap trend was also investigated by incorporating the Hubbard correction, optimizing the on-site Coulomb value in WH1 to U = 6 eV. This U value was extended to all other compositions, to take an approach that is independent of the amount of added Mo, the potential was applied over "d" orbital of oxygen atoms. The band structure showed in Figure 5 correspond to the results of DFT+U, which had the same gap trend; i.e. the gap decrease function of the Mo amount, obtaining 2.63 eV for WH1, 2.26 eV for WM25, 2.04 eV for WM50 and 1.98 eV for WM75 and indirect gaps. The gap reduction (and the enhanced efficiency in photocatalysis) by adding Mo is because of the extra bands below the conduction bands.

Our model correctly captures the current trend WH1 to WM75. Regarding MH1 structure, equal to DFT result, it was not possible to obtain semiconductor character. The clear relationship between band structures of the hydrated compound MH1 and its anhydrate analogy Mo_2O_3, which presents electronic gap (not shown), suggest that the measured gap could result from the combined presence of molybdenum oxide created by O vacancies. Different MH1 models with O vacancies were tested, despite the metallic character was not modified. In our employed models, it was not possible to investigate the importance of taking into account H atoms (thus dispersive forces) and its effect on the electronic gap, however will be presented in a future work.

In the Raman spectra, Figure 6 (a) reveals that all compounds synthetized by hydrothermal techniques (sample patterns were normalized), except MH1, show two strong peaks at 720 and 813 cm^{-1}, one medium peak at 280 cm^{-1} and one weak peak located at 336 cm^{-1}. There are very weak signals at 450 and 1000 cm^{-1}, respectively. The two strong peaks located at 720 and 813 cm^{-1} are due to stretching vibrations ν(W-O-W) of the bridging oxygen atoms, the peak at 336 cm^{-1} is characteristic of ς(O-W-O) deformation mode, and the weak signal at 1025 cm^{-1} could be attributed to the stretching mode of the terminal W=O double bond [13]. Because the solid solutions containing X= 0.25, 0.50, and 0.75 (WM25, WM50 and WM75) are quite similar to the X=0 (WH1), the Raman spectra show structural similarity of these samples. When the Mo atoms are in the crystal cell, there is a shift in the position of some bands. The bands located at 720 and 813 cm^{-1} gradually shift to 750 and 845 cm^{-1}, respectively, for the WM75 sample. At the same time these peaks become broader, which may be due to either disorder or loss of long distance translational periodicity (of high atomic number atoms) [14]. For MH1, the representative Raman bands of MoO_3*0.55H_2O are the frequency range of 200 to 1000 cm^{-1}. At 900 and 1000 cm^{-1}, we observe two bands that correspond to ν(O=Mo=O) and ν(Mo=O) stretching, respectively.

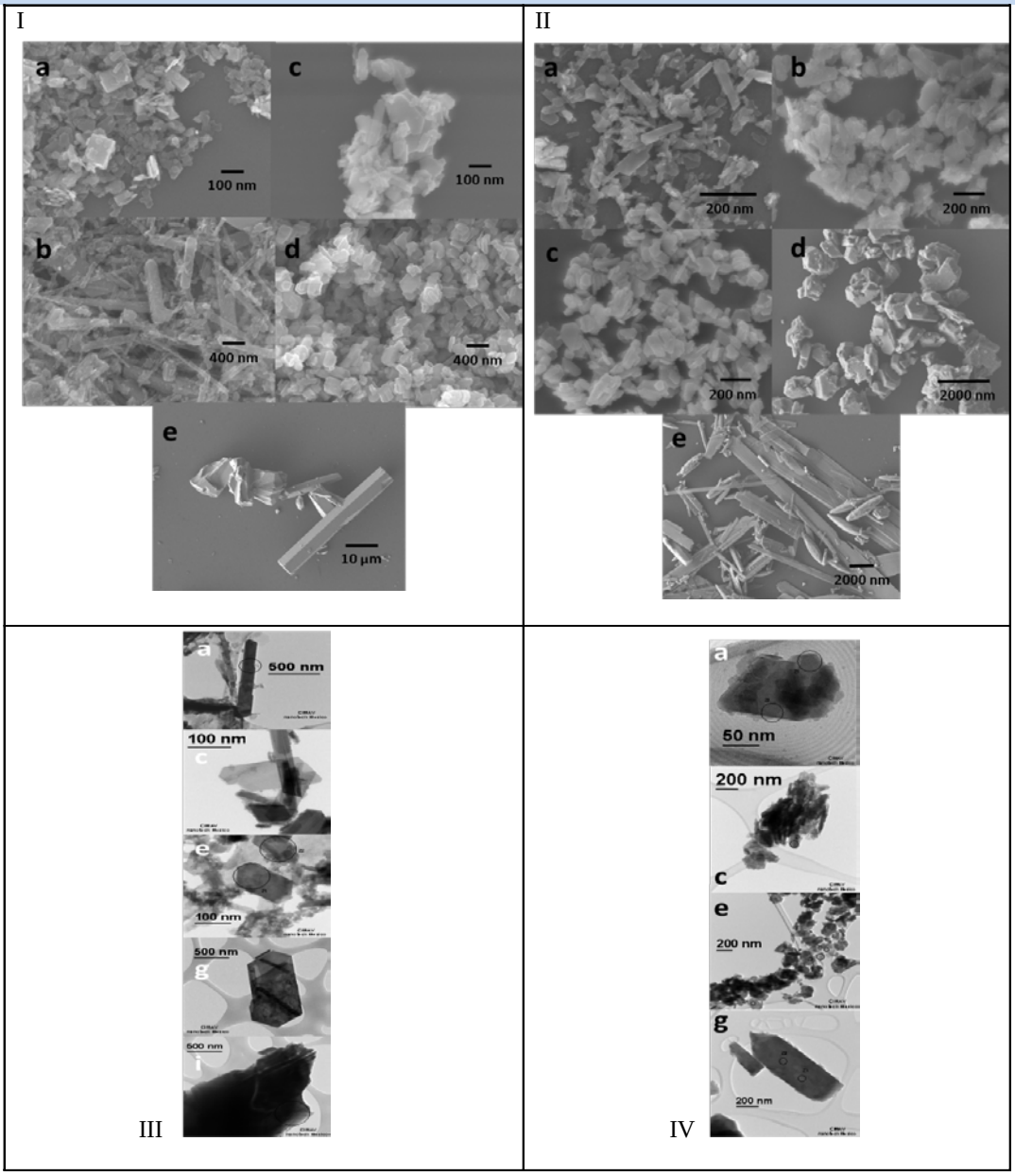

Fig. 3. (I) SEM images of (a) WH1, (b) WM25, (c) WM50, (d) WM75, and (e) MH1 compounds synthetized by hydrothermal technique. **(II)** SEM images of (a) WH1m, (b) WM25m, (c) WM50m, (d) WM75m, and (e) MH1m compounds synthetized by MW radiation. **(III)** TEM images of (a) WH1, (c) WM25, (e) WM50, (g) WM75 and (i) MH1 solid solutions synthetized by hydrothermal techniques. **(IV)** TEM images of (a) WH1m, (c) WM25m, (e) WM50m and (g) WM75m solid solutions synthetized by microwave radiation.

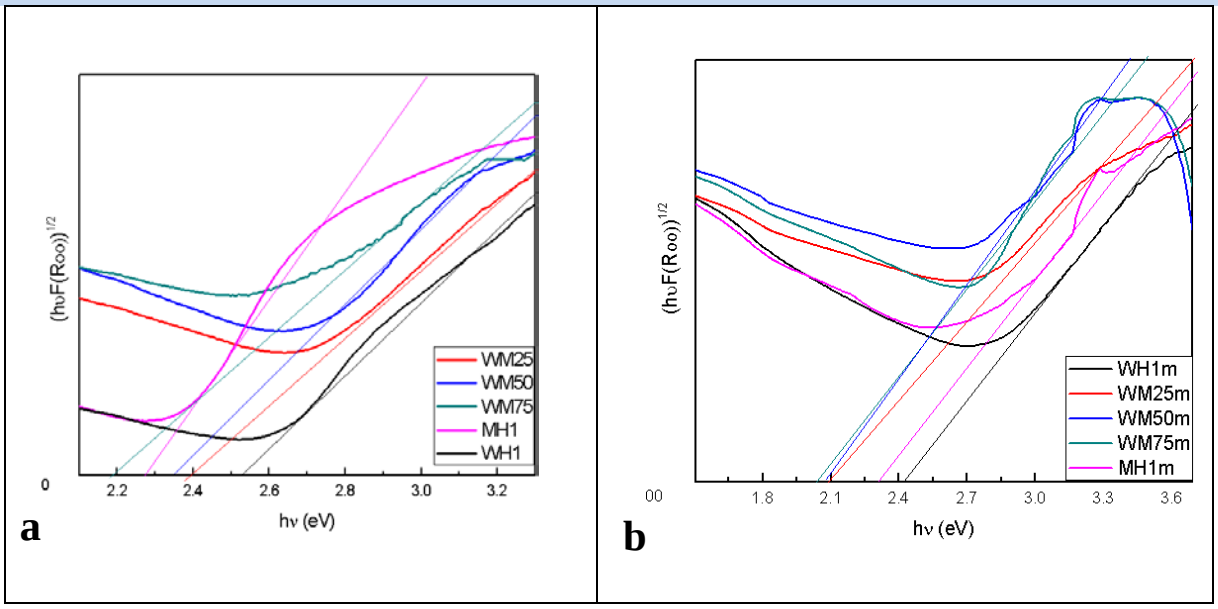

Fig. 4. Determination of band gap of each method: hydrothermal (a) and microwave (b) by drawing a line at $[F(R)h\gamma]^{1/2}=0$

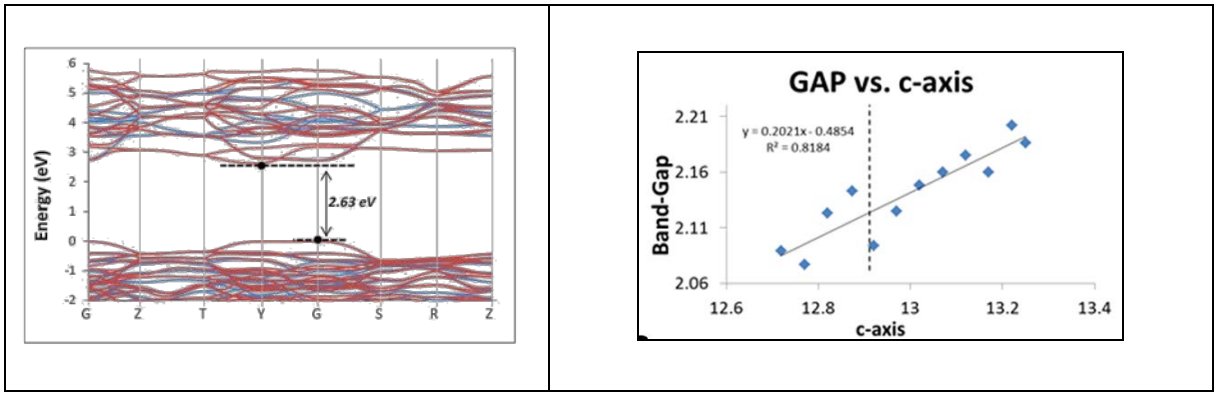

Fig. 5. Theoretical results obtained by DFT+U calculations: left side corresponds to band structure of conventional unit cell of WH1, right side corresponds to electronic valence after c-axis parameter is modified.

The band located at 700 cm^{-1} can be attributed to $\nu(OMo_2)$ and $\nu(OMo_3)$ stretching. The bands located at 400 and 500 cm^{-1} can be assigned to deformation modes. In the case of the band located at 340 cm^{-1}, it corresponds to a $\nu(Mo\text{-}OH_2)$ stretching. Below 300 cm^{-1}, we observe bands that are due to deformation and lattice modes. All assignments can be found in Table 2-I. In Figure 6 (b) shows the Raman spectra for compounds synthetized by microwave radiation. It reveals that all compounds, except MH1m, exhibit three strong peaks at 150, 670 and 800 cm^{-1}, one medium peak at 280 cm^{-1} and one weak peak located at 330 cm^{-1}. The two strong peaks located at 670 and 800 cm^{-1} are due to stretching vibrations ν(W-O-W) of the bridging oxygen atoms, the peak at 330 cm^{-1} is characteristic of ς(O-W-O) deformation mode. Because the solid solutions containing x= 0.25, 0.50, and 0.75 (WM25m, WM50m and WM75m) are quite similar to the x=0 (WH1m), the Raman spectra

shows structural similarity of these samples. When Molybdenum atoms substitutes Tungsten in the crystal lattice, there is a shift in the position of some bands. The bands located at 700 and 800 cm^{-1} gradually shift to 750 and 815 cm^{-1}, respectively, for the WM75m sample. At the same time

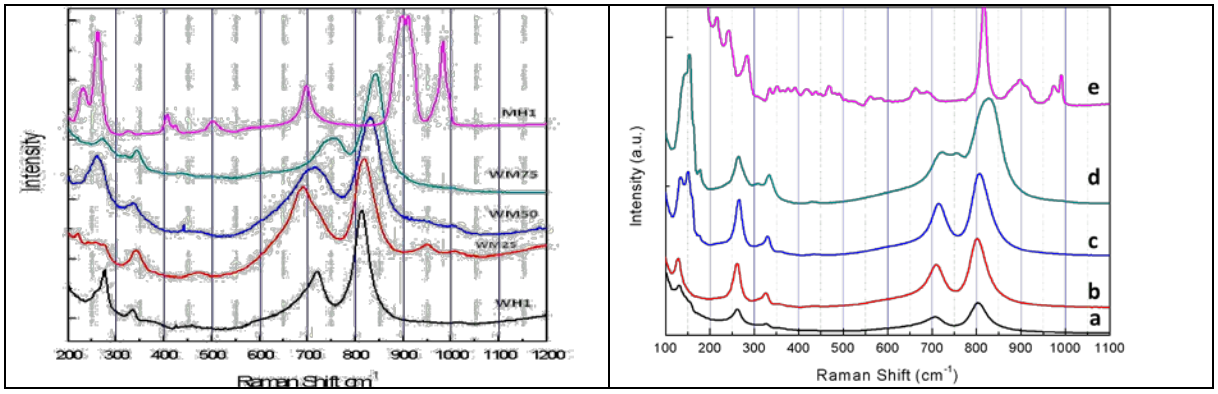

Fig. 6. (Right) Raman shifts of samples synthetized by hydrothermal synthesis: (a) WH1, (b) WM25, (c) WM50, (d) WM75 and (e) MH1. (Left) Raman shifts of samples synthetized by microwave radiation: (a) WH1m, (b) WM25m, (c) WM50m, (d) WM75m and (e) MH1m

Table 2-I: Raman frequencies (cm^{-1}) of $W_{1-x}Mo_xO_3*0.33H_2O$ and $MoO_3*0.55H_2O$ at ambient conditions.

WH1, WM25, WM50 and WM75 (cm^{-1})	$MoO_3*0.55H_2O$ (cm^{-1})	Assignment
	1000-900	ν(Mo=O) stretching ν(O=Mo=O) stretching
1000		W=O stretching
800-700		ν(W-O-W) stretching
	700	ν(OMo_2) stretching ν(OMo_3) stretching
	500-400	Deformation modes
350		ς(O-W-O) deformation
	340	ν(Mo-OH_2) stretching
	< 300	Deformation modes

these peaks become broader, which may be due to either disorder or loss of long distance translational periodicity (of high atomic number atoms) [15].

For the MH1m sample, the representative Raman bands of $MoO_3*0.55H_2O/Mo_2O_5$ (OH) are at the frequency range of 200 to 1000 cm^{-1}. At 900 and 1000 cm^{-1}, we observe two weak bands that correspond to ν(O=Mo=O) and ν(Mo=O) stretching, respectively. We

have a strong band at 800 cm^{-1} that corresponds to ν(Mo–O–Mo) stretching. The weak band located at 700 cm^{-1} can be attributed to ν(OMo_2) and ν(OMo_3) stretching. The bands located below 600 cm^{-1} can be assigned to deformation modes. All assignments can be found in Table 2-II.

Table 2-II. Raman frequencies (cm^{-1}) of $W_{1-x}Mo_xO_3$*0.33H_2O and $MoO_3$0*55H_2O/Mo_2O_5 compounds at ambient conditions.

WH1, WM25, WM50 and WM75 (cm^{-1})	MoO_3*055H_2O/Mo_2O_5 (OH) (cm^{-1})	Assignment
	1000-900	ν(Mo=O) stretching ν(O=Mo=O) stretching
	800	W=O stretching
800-670		ν(W-O-W) stretching
	700	ν(OMo_2) stretching ν(OMo_3) stretching
	<400	Deformation modes
330		ς(O-W-O) deformation

The photocatalityc activity evaluation of the compounds was monitored through the evolution of the hydrogen produced by the dissociation reaction of the water molecule via photocatalysis. Results are shown in Table 3. There was very little production of hydrogen and we believe it is because of the nature of WO_3 itself. We found studies that have shown that WO_3 is a visible light responsive photocatalyst with relatively narrow band-gap energy (2.4-2.8 eV) and a VB potential similar to that of Ag-TiO_2 [16]. Therefore, the oxidizing power of holes in the VB of WO_3 and TiO_2 are considered to be almost the same. However, pure WO_3 is not an efficient photocatalyst toward hydrogen production due its lower CB potential than hydrogen reduction potential, which limits the photocatalyst's ability to react with hydrogen of water molecule [17]. The low CB level also increases the recombination of photo-generated electron–hole pairs leading to minor photocatalytic activity.

Table 3. Photocatalytic hydrogen production through the dissociation of the water molecule under an Hg lamp (250W).

Compound	**Surface area m^2/g**	**H_2/g_{cat} μmoles**	**H_2/m^2 μmoles**	**Compound**	**Surface area m^2/g**	**H_2/g_{cat} μmoles**	**H_2/m^2 μmoles**
WH1	68	10	1.4	WH1m	43	10	2
WM25	46	11	2.3	WM25m	28	11	4
WM50	40	15	3.7	WM50m	19	15	8
WM75	15	20	13	WM75m	6	20	33
MH1	1	5	5	MH1m	6	5	8
Ag-TiO_2	140	180	13	Ag-TiO_2	140	180	13

4. Conclusion and recommendation

We have synthesized a series of $W_{1-x}Mo_xO_3*0.33H_2O$ solid solutions using hydrothermal and microwave radiation with controlled stoichiometry (x = 0, 0.25, 0.50, 0.75). The lattice of WH1 and WH1m ($WO_3*0.33H_2O$) can be substituted with up to 75% Mo without structural alteration. When we increase the content of Mo, the band gap of the $W_{1-x}Mo_xO_3*0.33H_2O$ structure narrowed from 2.62 to 2.10 eV. DFT+U calculations confirmed our experimental data and showed that gap narrow was due to added bands below conductions level of the original WH1 compound. Hydrogen production was reached after 4h of irradiation for each compound. Compound WM75m had the maximum amount produced that was 33 μmoles H_2/g_{cat}. We think that the properties of these enhanced compounds make them suitable for applications like photocatalysis or gas sensing.

Acknowledgments

The authors are thankful with Centro Nacional de Supercomputo (CNS) del Instituto Potosino de Investigacion Cientifica y Tecnologica (IPICyT) for computational resources and with Rodrigo Dominguez, CIMAV NANOTECH for support provided.

References

[1] Ni M, Leung MKH, Sumathy K, Leung DYC. Water electrolysis—a bridge between renewable resources and hydrogen. Proceedings of the International Hydrogen Energy forum, vol. 1, 25–28 May 2004, Beijing, PRC. p. 475–480.

[2] Hodes, G., Fonash, S.T., Heller, A., Miller, B.: In: Gerischer, H. (ed.) Advances in electrochemistry and electrochemical engineering. Wiley, New York (1985)

[3] Hardee, K., Bard, A.: Photoelectrochemical behaviour of several polycrystalline metal oxide electrodes in aqueous solutions. J. Electrochem. Soc. 123, 1024 (1976)

[4] Bahnemann, D.W., Hilgendorff, M., Memming, R.: Charge carrier dynamics at TiO_2 particles: reactivity of free and trapped holes. J. Phys. Chem. B 101, 4265–4275 (1997)

[5] Santato, C., Ulmann, M., Augustynski, J.: Enhanced visible light conversion efficiency using nanocrystalline WO3 films. Adv. Mater. 13, 511 (2001).

[6] Abe, R., Higashi, M., Domen, K.: Facile fabrication of an efficient oxynitride TaON photoanode for overall water splitting into H_2 and O_2 under visible light irradiation. J. Am. Chem. Soc. 132, 11828–11829 (2010)

[7] Hwang, Y.J., Boukai, A., Yang, P.D.: High density n-Si/n-TiO_2 core/shell nanowire arrays with enhanced photoactivity. Nano Lett. 9, 410–415 (2009)

[8] Baeck, S.H., Jaramillo, T.F., Brandli, C., McFarland, E.W.: Combinatorial electrochemical synthesis and characterization of tungsten-based mixed metal oxides. J. Comb. Chem. 4, 563 (2002)

[9] Khader, M.M., Vurens, G.H., Kim, I.K., Salmeron, M., Somorjai, G.A.: Photoassisted catalytic dissociation of water to produce hydrogen on partially reduced alpha.-iron(III) oxide. J. Am. Chem. Soc. 109, 3581 (1987)

[10] L. Zhou, J. Zhu, M. Yu, X. Huang, Z. Li, Y. Wang, and C. Yu, The Journal of Physical Chemistry C 114, 20947 (2010).

[11] F. Harb, B. Gerand, and M. Figlarz, C. R. Acad. Sci. Paris 303, 789 (1986).

[12] H. F., Solid State Ionics 32-3, 84 (1989).
[13] Daniel, M. F.; Desbat, B.; Lassegues, J. C.; Gerand, B.; Figlarz, M. J. Solid State Chem. 1987, 67, 235–247.
[14] Ph. Colomban, Stress- and Nanostructure-Imaging of Ceramic Fibers and Abradable Thermaln Barrier Coatings by Raman Microspectrometry : State of the Art and Perspectives, Ceram. Eng. & Sci. Proc. 21 (2000) 143.
[15] Ph. Colomban, Ceram. Eng. Sci. Proc. 21 (2000) 143.
[16] M. Miyauchi, M. Shibuya, Z. G. Zhao and Z. Liu, J. Phys. Chem. C, 2009, 113, 10642.
[17] M. Miyauchi, Phys. Chem. Chem. Phys., 2008, 10, 6258.